arXiv:nucl-th/9805018v1 7 May 1998

Three Body Bound State Calculations without Angular Momentum Decomposition

Ch. Elster, W. Schadow
Institute of Nuclear and Particle Physics, and Department of Physics, Ohio University, Athens, OH 45701

A. Nogga, W. Glöckle
Institute for Theoretical Physics II, Ruhr-University Bochum, D-44780 Bochum, Germany.

(February 9, 2008)

Abstract

The Faddeev equations for the three body bound state are solved directly as three dimensional integral equation without employing partial wave decomposition. The numerical stability of the algorithm is demonstrated. The three body binding energy is calculated for Malfliet-Tjon type potentials and compared with results obtained from calculations based on partial wave decomposition. The full three body wave function is calculated as function of the vector Jacobi momenta. It is shown that it satisfies the Schrödinger equation with high accuracy. The properties of the full wave function are displayed and compared to the ones of the corresponding wave functions obtained as finite sum of partial wave components. The agreement between the two approaches is essentially perfect in all respects.

I. INTRODUCTION

Three nucleon bound state calculations are traditionally carried out by solving Faddeev equations in a partial wave truncated basis, which leads to a set of a finite number of coupled equations in two variables for the amplitude. This is performed either in momentum space [1–3], in configuration space [4,5], or in a hybrid fashion using both spaces [6]. Though a few partial waves often provide qualitative insight, modern three nucleon bound state calculations need 34 or more different isospin, spin and orbital angular momentum combinations [3]. It appears therefore natural to avoid a partial wave representation completely and work directly with vector variables. This is common practice in bound state calculations of few nucleon systems based on variational [7] and Green's function Monte Carlo (GFMC) methods [8]. Those methods are normally carried out in configuration space, and while providing accurate results for the binding energy, the GFMC method samples the wave function only stochastically. Up to now the Faddeev equations have been solved applying vector variables only in configuration space for pure Coulomb bound state problems, the $e^-e^-e^+$ and $pp\mu^-$ systems [9]. There are other accurate techniques for solving for the three body binding energy based on correlated Hyperspherical Harmonic variational techniques [10,11] and the Gaussian basis coupled channel methods [12], which, however, all work with partial wave decomposition.

Our aim is to work directly with vector variables in the Faddeev scheme in momentum space. Under these circumstances the two-body t-matrices should also be determined directly as function of momentum vectors. This is not too difficult and has been recently demonstrated for two-body t-matrices based on Malfliet-Tjon type potentials [13]. The choice of momentum vectors as adequate variables is also suggested by the NN force. Here the dependence on momentum vectors can be rather simple, e.g., in the case of the widely used one-boson exchange force, whereas the partial wave representation of this force leads to rather complicated expressions [14].

Instead of first summing up two-body interactions to infinite order into two-body t-matrices and obtain connected kernel equations, the Schrödinger equation for the three nucleon (3N) bound state can be solved directly [15]. In that work the Schrödinger equation was solved in momentum space for identical particles without partial wave decomposition for Malfliet-Tjon type interactions. We do not want to follow this avenue but rather solve the Faddeev equations in momentum space directly in a three dimensional form. Section II describes our solution of the Faddeev equations as function of the momentum vectors and contrast this new approach with the standard form given in a partial wave decomposition. We work with spinless nucleons and thus formulate the Faddeev equations for a system of three bosons. In Section III we discuss details of our algorithm for solving the Faddeev equations for the three body bound state and demonstrate the stability of our numerical approach as well as compare to results obtained from partial wave based calculations. In Section IV we show properties of the Faddeev amplitude and the full wave function and demonstrate that the results obtained from the three dimensional approach and the ones coming from partial waves agree very well with each other. We compare momentum distributions and expectation values calculated within the two schemes. In Section V we demonstrate that the Schrödinger equation is fulfilled pointwise by the full wave function generated in the three dimensional approach. To the best of our knowledge this has never been demonstrated

before with this accuracy. We conclude in Section VI.

II. THREE-BODY BOUND STATE EQUATION

The bound state of three identical particles which interact via pairwise forces $V_i = V_{jk}$ ($ijk = 123$ and cyclic permutations thereof) is given by a Schrödinger equation which read in integral form

$$|\Psi\rangle = G_0 \sum_{i=1}^{3} V_i \, |\Psi\rangle. \tag{2.1}$$

Here the free propagator is given by $G_0 = (E - H_0)^{-1}$, and H_0 stands for the free Hamiltonian. Introducing Faddeev components $|\Psi\rangle = \sum\limits_{i=1}^{3} |\psi_i\rangle$ with $|\psi_i\rangle = G_0 \, V_i \, |\Psi\rangle$ leads to the three coupled integral equations

$$|\psi_i\rangle = G_0 \, t_i \sum_{j \neq i} |\psi_j\rangle. \tag{2.2}$$

The operator t_i describes the two-body t-matrix in the subsystem jk. If we consider identical particles (here bosons, since we are omitting spin), the three nucleon wave function $|\Psi\rangle$ has to be totally symmetric. As a consequence, $|\psi_1\rangle$, $|\psi_2\rangle$, and $|\psi_3\rangle$ are identical in their functional form, only the particles are permuted. Thus it is sufficient to consider only one component

$$|\psi\rangle = G_0 \, t \, P \, |\psi\rangle, \tag{2.3}$$

where the arbitrarily chosen index 1 is dropped. In this case the permutation operator P is given as $P = P_{12}P_{23} + P_{13}P_{23}$. The complete three nucleon wave function is then given as

$$|\Psi\rangle = (1 + P) \, |\psi\rangle. \tag{2.4}$$

In order to solve Eq. (2.3) in momentum space we introduce standard Jacobi momenta

$$\begin{aligned} \mathbf{p}_i &= \tfrac{1}{2}(\mathbf{k}_j - \mathbf{k}_k) \\ \mathbf{q}_i &= \tfrac{2}{3}(\mathbf{k}_i - \tfrac{1}{2}(\mathbf{k}_j + \mathbf{k}_k)), \end{aligned} \tag{2.5}$$

where $ijk = 123$ and cyclic permutations thereof. With the arbitrary choice $i = 1$ and omitting the index 1 for clarity of presentation Eq. (2.3) reads

$$\langle \mathbf{pq}|\psi\rangle = \frac{1}{E - \frac{1}{m}p^2 - \frac{3}{4m}q^2} \, \langle \mathbf{pq}|tP|\psi\rangle \tag{2.6}$$

with

$$\langle \mathbf{pq}|t \, P|\psi\rangle = \int d^3q' \, d^3p' \, d^3q'' \, d^3p'' \; \langle \mathbf{pq}|t|\mathbf{p'q'}\rangle \, \langle \mathbf{p'q'}|P|\mathbf{p''q''}\rangle \, \langle \mathbf{p''q''}|\psi\rangle. \tag{2.7}$$

The momentum states are normalized according to $\langle \mathbf{p'q'}|\mathbf{pq}\rangle = \delta^3(\mathbf{p'} - \mathbf{p}) \, \delta^3(\mathbf{q'} - \mathbf{q})$. The Jacobi momenta in the different two-body subsystems (13) and (12) are expressed through those defined in the subsystem (23) via

$$
\begin{aligned}
\mathbf{q}_1 &= -\mathbf{p}_2 - \tfrac{1}{2}\mathbf{q}_2 \\
\mathbf{p}_1 &= -\tfrac{1}{2}\mathbf{p}_2 + \tfrac{3}{4}\mathbf{q}_2 \\
\mathbf{q}_1 &= \mathbf{p}_3 - \tfrac{1}{2}\mathbf{q}_3 \\
\mathbf{p}_1 &= -\tfrac{1}{2}\mathbf{p}_3 - \tfrac{3}{4}\mathbf{q}_3 .
\end{aligned} \tag{2.8}
$$

This allows to evaluate the permutation operator given in Eq. (2.7) as

$$
\begin{aligned}
\langle \mathbf{p}'\mathbf{q}'|P|\mathbf{p}''\mathbf{q}''\rangle &= \langle \mathbf{p}'\mathbf{q}'|\mathbf{p}''\mathbf{q}''\rangle_2 + \langle \mathbf{p}'\mathbf{q}'|\mathbf{p}''\mathbf{q}''\rangle_3 \\
&= \delta^3(\mathbf{p}' + \tfrac{1}{2}\mathbf{q}' + \mathbf{q}'')\, \delta^3(\mathbf{p}'' - \mathbf{q}' - \tfrac{1}{2}\mathbf{q}'') \\
&\quad + \delta^3(\mathbf{p}' - \tfrac{1}{2}\mathbf{q}' - \mathbf{q}'')\, \delta^3(\mathbf{p}'' + \mathbf{q}' + \tfrac{1}{2}\mathbf{q}''),
\end{aligned} \tag{2.9}
$$

where the indices 2 and 3 indicate the corresponding subsystem. Inserting this relation into Eq. (2.7) and then into Eq. (2.6) leads to the expression for the Faddeev amplitude which serves as starting point for our numerical calculations,

$$
\langle \mathbf{p}\mathbf{q}|\psi\rangle = \frac{1}{E - \frac{1}{m}p^2 - \frac{3}{4m}q^2} \int d^3q'\; t_{\rm s}(\mathbf{p}, \tfrac{1}{2}\mathbf{q} + \mathbf{q}', E - \tfrac{3}{4m}q^2)\, \langle \mathbf{q} + \tfrac{1}{2}\mathbf{q}', \mathbf{q}'|\psi\rangle . \tag{2.10}
$$

Here $t_{\rm s}(\mathbf{p}, \mathbf{q}, E)$ is the symmetrized two-nucleon t-matrix,

$$
t_{\rm s}(\mathbf{p}, \mathbf{q}, E) = t(\mathbf{p}, \mathbf{q}, E) + t(-\mathbf{p}, \mathbf{q}, E). \tag{2.11}
$$

We would like to mention that the so obtained Faddeev amplitude fulfills the symmetry relation $\psi(\mathbf{pq}) = \psi(-\mathbf{pq})$, as can be seen from Eq. (2.10).

In Eq. (2.10) the Faddeev amplitude $\psi(\mathbf{pq})$ is given as function of vector Jacobi momenta and obtained as solution of a three dimensional integral equation. For the ground state $\psi(\mathbf{pq})$ is a scalar and thus depends only on the magnitudes of $\mathbf{p}$ and $\mathbf{q}$ and the angle between those vectors. In order to solve this equation directly without inserting partial wave projections, we have to define a coordinate system. We choose the vector $\mathbf{q}$ parallel to the z-axis and express the remaining vectors $\mathbf{p}$ and $\mathbf{q}'$ with respect to $\mathbf{q}$. As variables we have the magnitudes of the vectors as well as the following angle relations,

$$
\begin{aligned}
x &\equiv \hat{\mathbf{p}} \cdot \hat{\mathbf{q}} = \cos\theta \\
x' &\equiv \hat{\mathbf{q}}' \cdot \hat{\mathbf{q}} = \cos\theta' \\
y &\equiv \hat{\mathbf{p}} \cdot \hat{\mathbf{q}}' = \cos\gamma ,
\end{aligned} \tag{2.12}
$$

where

$$
\cos\gamma = \cos\theta\cos\theta' + \sin\theta\sin\theta'\cos(\varphi - \varphi') = xx' + \sqrt{1-x^2}\,\sqrt{1-x'^2}\,\cos\varphi' . \tag{2.13}
$$

To arrive at the last relation we took advantage of the freedom of choice for one azimuthal angle and set $\varphi = 0$. We have this freedom due to the φ' integration over the full 2π interval. With these variables Eq. (2.10) can be explicitly written as

$$
\begin{aligned}
\psi(p,q,x) = \frac{1}{E - \frac{1}{m}p^2 - \frac{3}{4m}q^2} & \int_0^\infty dq' q'^2 \int_{-1}^{1} dx' \int_0^{2\pi} d\varphi' \\
& \times t_{\rm s}\left(p, \sqrt{\tfrac{1}{4}q^2 + q'^2 + qq'x'}, \frac{\frac{1}{2}qx + q'y}{|\frac{1}{2}\mathbf{q} + \mathbf{q}'|}; E - \tfrac{3}{4m}q^2\right) \\
& \times \psi\left(\sqrt{q^2 + \tfrac{1}{4}q'^2 + qq'x'}, q', \frac{qx' + \frac{1}{2}q'}{|\mathbf{q} + \frac{1}{2}\mathbf{q}'|}\right),
\end{aligned} \tag{2.14}
$$

where $|\frac{1}{2}\mathbf{q}+\mathbf{q}'| = \sqrt{\frac{1}{2}q^2+q'^2+qq'x'}$ and $|\mathbf{q}+\frac{1}{2}\mathbf{q}'| = \sqrt{q^2+\frac{1}{4}q'^2+qq'x'}$.
The above equation, Eq. (2.14), is the starting point for our numerical algorithms, and the details will be described in the next Section.

In a standard partial wave representation [16] Eq. (2.14) is replaced by a set of coupled two-dimensional integral equations

$$\psi_l(p,q) = \frac{1}{E-\frac{1}{m}p^2-\frac{3}{4m}q^2} \times \sum_{l'} \int_0^\infty dq' q'^2 \int_{-1}^{1} dx' \; \frac{t_l(p,\pi_1,E-\frac{3}{4m}q^2)}{\pi_1^l} \; G_{ll'}(q,q',x') \; \frac{\psi'_l(\pi_2,q')}{\pi_2^{l'}}, \tag{2.15}$$

where

$$\pi_1 = \sqrt{q'^2+\frac{1}{4}q^2+qq'x'}$$
$$\pi_2 = \sqrt{q^2+\frac{1}{4}q'^2+qq'x'}. \tag{2.16}$$

Here $G_{ll'}(q,q',x')$ together with the shifted arguments π_1 and π_2 are the partial wave representation of the permutation operator. The explicit form of $G_{ll'}(q,q',x')$ can be found in Ref. [16]. However, the expression given in this reference is more complicated due to spin and isospin variables. For the convenience of the reader we give $G_{ll'}(q,q',x')$ defined for general total orbital angular momentum in Appendix A explicitly. The quantities t_l are the partial wave projected two-body t-matrices. Due to the symmetry requirement of the Faddeev amplitude, l runs over even values only. The infinite set of coupled integral equations given in Eq. (2.15) is truncated in actual calculations at a sufficiently high value of l. The full Faddeev amplitude $\psi(p,q,x)$ reads then

$$\psi(p,q,x) = \sum_l \frac{\sqrt{2l+1}}{4\pi} P_l(x) \, \psi_l(p,q). \tag{2.17}$$

From the Faddeev amplitude $\psi(\mathbf{p},\mathbf{q})$ the three nucleon wave function is obtained by adding the components defined in the different subsystems as given in Eq. (2.4). After evaluating the permutation operator P, the wave function is given as

$$\Psi(\mathbf{p},\mathbf{q}) = \psi(\mathbf{p},\mathbf{q}) + \psi(-\tfrac{3}{4}\mathbf{q}-\tfrac{1}{2}\mathbf{p}, \mathbf{p}-\tfrac{1}{2}\mathbf{q}) + \psi(\tfrac{3}{4}\mathbf{q}-\tfrac{1}{2}\mathbf{p}, -\mathbf{p}-\tfrac{1}{2}\mathbf{q}). \tag{2.18}$$

Already here we see that $\Psi(\mathbf{p},\mathbf{q}) = \Psi(-\mathbf{p},\mathbf{q})$, provided the Faddeev components fulfill this symmetry. Again the momentum $\mathbf{q}$ is chosen in the direction of the z-axis and after some algebra the explicit expression for the three nucleon wave function reads

$$\begin{aligned}\Psi(p,q,x) = {} & \psi(p,q,x) \\ & + \psi\left(\tfrac{1}{2}\sqrt{\tfrac{9}{4}q^2+p^2+3pqx}, \sqrt{p^2+\tfrac{1}{4}q^2-pqx}, \frac{\frac{3}{8}q^2-\frac{1}{2}p^2-\frac{1}{2}pqx}{|-\frac{3}{4}\mathbf{q}-\frac{1}{2}\mathbf{p}||\mathbf{p}-\frac{1}{2}\mathbf{q}|}\right) \\ & + \psi\left(\tfrac{1}{2}\sqrt{\tfrac{9}{4}q^2+p^2-3pqx}, \sqrt{p^2+\tfrac{1}{4}q^2+pqx}, \frac{-\frac{3}{8}q^2+\frac{1}{2}p^2-\frac{1}{2}pqx}{|\frac{3}{4}\mathbf{q}-\frac{1}{2}\mathbf{p}||-\mathbf{p}-\frac{1}{2}\mathbf{q}|}\right),\end{aligned} \tag{2.19}$$

where the magnitudes in the denominators of the angle variables are given by

$$\begin{aligned} \left|\tfrac{3}{4}\mathbf{q} \pm \tfrac{1}{2}\mathbf{p}\right| &= \tfrac{1}{2}\sqrt{\tfrac{9}{4}q^2 + p^2 \pm 3pqx} \\ \left|\mathbf{p} \pm \tfrac{1}{2}\mathbf{q}\right| &= \sqrt{p^2 + \tfrac{1}{4}q^2 \pm pqx}. \end{aligned} \tag{2.20}$$

The wave function is normalized according to

$$\int d^3p\, d^3q\; \Psi^2(\mathbf{p},\mathbf{q}) = 1, \tag{2.21}$$

which reads explicitly

$$8\pi^2 \int_0^\infty p^2 dp \int_0^\infty q^2 dq \int_{-1}^{1} dx\; \Psi^2(p,q,x) = 1. \tag{2.22}$$

The properties of the three nucleon wave function will be studied in Section IV.

In a partial wave representation Eq. (2.18) takes the form

$$\Psi(p,q,x) = \sum_l \frac{\sqrt{2l+1}}{4\pi} P_l(x)\, \Psi_l(p,q), \tag{2.23}$$

where

$$\Psi_l(p,q) = \psi_l(p,q) + \sum_{l'} \int_{-1}^{1} dx\, \tilde{G}_{ll'}(p,q,x)\, \psi_{l'}(\tilde{\pi}_1, \tilde{\pi}_2) \tag{2.24}$$

and

$$\begin{aligned} \tilde{\pi}_1 &= \sqrt{\tfrac{1}{4}p^2 + \tfrac{9}{16}q^2 + \tfrac{3}{4}qpx} \\ \tilde{\pi}_2 &= \sqrt{p^2 + \tfrac{1}{4}q^2 - qpx}. \end{aligned} \tag{2.25}$$

The quantity $\tilde{G}_{ll'}(p,q,x)$, which results from applying the permutation operator, can be found in Ref. [17], but should be considered without spin and isospin factors. The resulting expression for the here considered bosonic case is given in Appendix A.

III. CALCULATION OF THE THREE-BODY BINDING ENERGY

For our model calculations we use Yukawa interactions of Malfliet-Tjon [18] type,

$$V(\mathbf{p}',\mathbf{p}) = \frac{1}{2\pi^2}\left(\frac{V_{\rm R}}{(\mathbf{p}'-\mathbf{p})^2 + \mu_{\rm R}^2} - \frac{V_{\rm A}}{(\mathbf{p}'-\mathbf{p})^2 + \mu_{\rm A}^2}\right). \tag{3.1}$$

We study two different types of pairwise forces, a purely attractive Yukawa interaction and a superposition of a short-ranged repulsive and a long-ranged attractive Yukawa interaction. In order to be able to compare our calculations with results obtained by other methods we use the Malfliet-Tjon potentials MT-IV and MT-V [18]. However, we use slightly different

parameters as given in Ref. [18] to compare with Refs. [5,19] as well as [4] and give our parameters in Table I. The calculated values for the deuteron binding energy are $E_{\rm d} = -2.2087$ MeV for the MT-IV potential and $E_{\rm d} = -0.3500$ MeV for the MT-V potential, respectively. We also need to point out that we calculate the potentials as functions of vector momenta and thus define the interaction as a truly local force acting in all partial waves.

With this interaction we first solve the Lippmann-Schwinger equation for the fully-off-shell two-nucleon t-matrix directly as function of the vector variables as described in detail in Ref. [13]. The so obtained t-matrix is then symmetrized to get $t_{\rm s}(p', p, x; E - \frac{3}{4m}q^2)$. We would like to point out that after having solved the Lippmann-Schwinger equation on Gaussian grids for p, p', and x, we solve the integral equation again to obtain the t-matrix at points $x = \pm 1$. Thus, when iterating Eq. (2.14), we do not have to extrapolate numerically to angle points x of $t_{\rm s}(p', p, x; E - \frac{3}{4m}q^2)$, which can very well be located outside the upper or lower boundary of the Gaussian grid of the t-matrix.

The eigenvalue equation, Eq. (2.14), is solved by iteration. Schematically this can be written as

$$\lambda\, \psi = \mathcal{K}(E)\, \psi, \tag{3.2}$$

and we search for E such that $\lambda = 1$. The functional behavior of $\mathcal{K}(E)$ is determined by the two-body t-matrix, and $\lambda = 1$ is always the largest positive eigenvalue regardless of the two-nucleon potential being employed. For this reason the simple iteration starting with an essentially arbitrary vector is sufficient. We start with a vector $\psi(p, q, x) \sim 1/((1+p^2)(1+q^2))$ and stop the iteration when Eq. (3.2) is fulfilled with a relative accuracy of 10^{-10} at each point (p, q, x).

In order to solve the eigenvalue equation, Eq. (2.14), for the Faddeev component $\psi(p, q, x)$ we use Gaussian grid points in p, q, and x, though only the q-variable is a true integration variable. Typical grid sizes are $97 \times 97 \times 42$ to obtain an accuracy in the binding energy of 4 significant figures. This grid contains x points for $x = \pm 1$ as well as the points $p = 0$ and $q = 0$. The iteration of Eq. (2.14) requires a two-dimensional interpolation on $\psi(p, q, x)$ in the variables p and x. By including the additional grid points, we avoid the extrapolation outside the Gaussian grid. The q'-integration in Eq. (2.14) is cut off at a value of $q_{\rm max} = 20$ fm^{-1}. The integration interval is divided into two parts, $(0, q_0) \cup (q_0, q_{\rm max})$, in which we use Gaussian quadrature with NQ1 and NQ2 points respectively. The value for q_0 is chosen to be 10 fm^{-1}. Typical values for NQ1 and NQ2 are 64 and 32 to obtain the above mentioned accuracy. For the distribution of quadrature points we use the maps given in Ref. [20]. The x' integration requires typically at least 32 integration points, while for the φ' integration 20 points are already sufficient. The φ' integration acts only on $t_{\rm s}$ and can thus be carried out before starting to solve Eq. (2.14). The p variable is also defined in an interval $(0, p_0) \cup (p_0, p_{\rm max})$, where p_0 is chosen to be 9 fm^{-1} and $p_{\rm max} = 60$ fm^{-1}. The two intervals contain NP1 and NP2 points, and we choose NP1 = NQ1 and NP2 = NQ2 respectively.

The momentum dependencies given in Eq. (2.14) suggest that we solve the two-body t-matrix $t_{\rm s}(p, p', x; \varepsilon)$ on the momentum grid p and p' for the energies $\varepsilon = E - \frac{3}{4m}q^2$ dictated by the same q-grid. It turns out that it is sufficient to choose for the variable x the same grid which is used for solving the two-body Lippmann-Schwinger equation for $t_{\rm s}(p, p', x; \varepsilon)$. In order to obtain the second momentum and the angle for $t_{\rm s}(p, p', x; \varepsilon)$ required in the

integration of Eq. (2.14), we have to carry out two-dimensional interpolations. We use the Cubic Hermitean splines of Ref. [21]. The functional form of those splines is described in detail in Appendix B of this reference and shall not be repeated here. We find these splines superior to standard B-splines [22] in capturing the peak structure of the two-body t-matrix, which occurs for off-shell momenta $p \simeq p'$. In Fig. 1 the off-shell structure of the symmetrized t-matrix $t_{\rm s}(p,p',x;\varepsilon)$ for a center-of-mass (c.m.) energy $\varepsilon = -50$ MeV and an off-shell momentum $p' = 0.75$ fm^{-1} is displayed. The two steep dips at $x = \pm 1$ dominate the off-shell structure and are present for all off-shell momenta $p \simeq p'$. An additional advantage of the Cubic Hermitean splines is their computational speed, which is an important factor, since the integral in Eq. (2.14) requires a very large number of interpolations. Finally, to obtain the Faddeev component entering the integration we also need a two-dimensional interpolation and use the same as for the t-matrix.

In Table II we show the convergence of the three nucleon binding energy as function of the number of grid points for the Malfliet-Tjon potentials MT-V and MT-IV. We use the potential parameters as given in Table I. In Table III the convergence of the energy eigenvalues for the same potentials resulting from the solution of the partial wave Faddeev equation for an optimized set of p and q grid points as function of the angular momentum l is given.

As demonstrated in Table II, the calculation of the three nucleon binding energy using the Malfliet-Tjon potential V converges to a value of $E_{\rm t} = -7.7365$ MeV. The solution of the Faddeev equation in partial waves converges to $E_{\rm t} = -7.7366$ MeV. Here convergence is reached for $l = 12$. Both of the here calculated values for the potential MT-V are in excellent agreement with the value $E_{\rm t} = -7.7366$ MeV given in Ref. [19]. The agreement with the slightly older calculation of Ref. [4], which uses 6 partial waves for the potential and yielding $E_{\rm t} = -7.736$ MeV is also excellent. The agreement with the value $E_{\rm t} = -7.7365$ MeV obtained from a the paired potential basis calculation [10] gives the same excellent agreement.

For the purely attractive potential MT-IV our calculations of the binding energy converge to $E_{\rm t} = -25.050$ MeV as shown in Table II. The solution based on partial wave decomposition converges to $E_{\rm t} = -25.057$ MeV for $l = 12$. Both values are also in very good agreement with the value $E_{\rm t} = -25.05$ MeV quoted in Ref. [15]. As we can see from these comparisons to calculations of the three nucleon binding energy based on the solution of the Faddeev equations in partial waves, our results provide the same accuracy while the numerical procedures are actually easier to implement. In the three dimensional case there is only one single equation to be solved, whereas in the partial wave case one has a set of coupled equations with a kernel containing relatively complicated geometrical expressions $G_{ll'}(p,p',x)$ and $t_l(p,p',x)$ matrices to larger values of l. The latter ones are driven by the partial wave projected potential matrix elements $V_l(p,p')$, which require for large l-values and larger p-values (80-100 fm^{-1}) great care to be generated reliably. In contrast, the t-matrices are generated more easily as functions of vector momenta from the original potential. Once an accurate and fast two dimensional interpolation scheme is established, the implementation of Eq. (2.14) is rather simple.

IV. THE THREE NUCLEON WAVE FUNCTION

A. Properties

When solving Eq. (2.14) for the bound state, we obtain the Faddeev component $\psi(p,q,x)$, and the symmetry relation for the Faddeev component reads explicitly $\psi(p,q,x) = \psi(p,q,-x)$. Note that in Eq. (2.14) this symmetry is only fulfilled because of the φ-integration over the complete 2π interval. We verified that our numerical solution satisfies this symmetry with high accuracy. In fact, this symmetry property can be implemented in the iteration of Eq. (2.14) to cut down the size of the field $\psi(p,q,x)$ and thus save time and memory when computing the integral. We would like to remark that for the initial calculations we did not take advantage of this symmetry property in order to use the numerical verification as a test for the accuracy of the integration and interpolation.

In Fig. 2 we display magnitude of the Faddeev component at a fixed angle, $\psi(p,q,x=1)$ obtained from a calculation based on the MT-V potential. The norm is chosen such that $\langle\Psi|\Psi\rangle = 3\,\langle\psi|\Psi\rangle = 1$, where Ψ is the full 3N wave function as given in Eq. (2.18). The major contributions to $\psi(p,q,x)$ arise from momenta p and q less than 1.5 fm^{-1}. It also turns out that the dependence of $\psi(p,q,x)$ on the angle between the Jacobi momenta $\mathbf{p}$ and $\mathbf{q}$ is so weak that it can only be detected on a logarithmic scale but not when comparing linear plots at different values of x. This is understandable, since the admixture of the $l > 0$ partial waves into the Faddeev amplitude is less than 0.01%. To show this we choose the normalization differently from above as

$$1 = \int\limits_{-1}^{1} dx \int\limits_{0}^{\infty} dp\, p^2 \int\limits_{0}^{\infty} dq\, q^2\, \psi^2(p,q,x) \tag{4.1}$$

or, according to Eq. (2.17)

$$\begin{aligned} 1 &= \sum_l \int\limits_{0}^{\infty} dp\, p^2 \int\limits_{0}^{\infty} dq\, q^2\, \psi_l^2(p,q) \\ &\equiv \sum_l F_l. \end{aligned} \tag{4.2}$$

Similar we define for the full wave function

$$\begin{aligned} 1 &= \sum_l \int\limits_{0}^{\infty} dp\, p^2 \int\limits_{0}^{\infty} dq\, q^2\, \Psi_l^2(p,q) \\ &\equiv \sum_l W_l. \end{aligned} \tag{4.3}$$

The partial wave contributions F_l and W_l are given in Table IV for the different l values.

The logarithmic presentation in Fig. 2 allows to see not only the smooth bell-like decrease of the Faddeev amplitude for p and q less than 1.5 fm^{-1} but also the deep valleys caused by the node lines of the amplitude. A more detailed inspection of the Faddeev amplitude is presented in Fig. 3. Here the partial wave amplitudes $\psi_l(p,q)$ are projected out numerically from the full amplitude $\psi(p,q,x)$ and compared to the amplitudes $\psi_l(p,q)$ directly determined from the coupled set of equations given in Eq. (2.15). We show contour plots for the l values 0, 2, and 4. One can see that for the higher l values the maximum of the partial wave

amplitudes moves to larger p and q values. It is also apparent from the figure that the graphs representing the three dimensional calculation and those for ones based on partial waves are nearly everywhere indistinguishable. This underlines the accuracy and consistency in the numerical realization of both schemes. Only for $l = 4$ and very small q-values deviations occur. There the contour lines have to be almost parallel to the p-axis, indicating the proper threshold behavior for very small q. This is not the case in the 3D approach. However, the value of the amplitude is smaller by 6 orders of magnitude compared to the value of the the $l = 0$ amplitude at these values. In both cases we hit numerical inaccuracies here for the number of grid points chosen.

The evaluation of the 3N wave function according to Eq. (2.18) requires interpolations in three dimensions. We would like to reiterate here, that for the solution of the Faddeev equation, Eq. (2.14), only two-dimensional interpolations are required. To carry out the 3D interpolation we use standard B-splines as given in [22]. In case of the wave function B-splines turned out to be slightly more accurate on the given grids compared to the Cubic Hermite splines. Since the wave function is calculated only once, the computational speed is not an issue here.

The absolute value of the total wave function $\Psi(p, q, x)$ calculated from the MT-V potential for a fixed angle $x = 1$ is displayed in Fig. 4. This wave function has a smooth shape and is significant in size only for p and q values smaller than 1.5 fm^{-1}. It is interesting to see that the shape of the wave function is quite similar to that of the Faddeev amplitude of Fig. 2. The function values are of course different.

In Fig. 5 the partial wave projected amplitudes $\Psi_l(p, q)$ are displayed as contour plots for $l = 0$, 2, and 4. The left column contains the $\Psi_l(p, q)$ obtained from the solution of Eq. (2.19), whereas the right column contains $\Psi_l(p, q)$ calculated directly in partial waves from Eq. (2.24). Again, both plots are nearly everywhere indistinguishable, underlining the accuracy and consistency in the numerical realization of both schemes. For $l = 4$ the contour plot for $\Psi_4(p, q)$ calculated in partial waves show small irregularities for p values larger than 5 fm^{-1} and q close to 0. These irregularities are missing in the projections obtained from the full 3D solution, but again as pointed out above the 3D solution is not correct there either.

In Fig. 6 we show the wave function $\Psi(p, q, x)$ calculated from the MT-IV potential. A comparison with Fig. 4 shows that for the purely attractive potential the significant pieces of the wave function are more shifted to slightly larger momenta p and q. This is consistent with the larger binding energy given by the MT-IV potential, which causes the 3N system to be tighter bound when viewed in configuration space and thus giving a more extended structure in momentum space. Due to the lack of repulsion this wave function does not change sign.

B. Momentum Distributions and Expectation Values

In applications one does not access the wave function directly but rather only certain matrix elements thereof. One example, which can be 'measured' at least approximately in electron scattering is the momentum distribution, the probability to find a nucleon with momentum q in the nucleus. In our case this is given by

$$n(q) = 2\pi q^2 \int_0^\infty dp\, p^2 \int_{-1}^{1} dx\, \Psi^2(p,q,x)$$
$$= \frac{1}{4\pi} \sum_l q^2 \int_0^\infty dp\, p^2\, \Psi_l^2(p,q,x). \tag{4.4}$$

It is of interest to see how the sum of the partial wave form approaches the expression evaluated directly from $\Psi(p,q,x)$. In Fig. 7 we display the momentum distribution obtained from $\Psi(p,q,x)$ together with the partial wave sums corresponding to different l. The small q values are dominated by the $l=0$ part. However, for a correct representation of $n(q)$ for larger q larger l values are required. While for $q \leq 3$ fm^{-1} $l=0$ and 2 are sufficient, at $q \sim 10$ fm^{-1} one needs l values as large as 8.

Another interesting test for the numerical accuracy is the comparison of a complementary quantity, namely

$$\hat{n}(p) = 2\pi\ p^2 \int_0^\infty dq\, q^2 \int_{-1}^{1} dx\, \Psi^2(p,q,x)$$
$$= \frac{1}{4\pi} \sum_l p^2 \int_0^\infty dq\, q^2\, \Psi_l^2(p,q,x). \tag{4.5}$$

This quantity does not seem to be easily accessible experimentally. The momentum distribution $\hat{n}(p)$ as obtained from $\Psi(p,q,x)$ together with its partial wave sums of different l is shown in Fig. 8. Here higher l values are mostly needed to fill in the dip at 2 fm^{-1}.

A less detailed test for the quality of the 3N wave function is the evaluation of the expectation value $\langle\Psi|H|\Psi\rangle \equiv \langle H\rangle$ and compare this value to the previously calculated eigenvalues. Explicitly we evaluate the following expression

$$\langle\Psi|H|\Psi\rangle = \langle\Psi|H_0|\Psi\rangle + \langle\Psi|V|\Psi\rangle = 3\,\langle\psi|H_0|\Psi\rangle + 3\,\langle\Psi|V_1|\Psi\rangle, \tag{4.6}$$

where

$$\langle\psi|H_0|\Psi\rangle = 8\pi^2 \int_0^\infty dp \int_0^\infty dq \left[\frac{1}{m}p^2 + \frac{3}{4m}q^2\right] \int_{-1}^{1} dx\, p^2\, q^2\, \psi(p,q,x)\, \Psi(p,q,x) \tag{4.7}$$

and

$$\langle\Psi|V_1|\Psi\rangle = 8\pi^2 \int_0^\infty dp\, p^2 \int_0^\infty dq\, q^2 \int_0^\infty dp'\, p'^2 \int_{-1}^{1} dx \int_{-1}^{1} dx'$$
$$\times\, \Psi(p,q,x)\, v_1(p,p',x,x')\, \Psi(p',q,x'). \tag{4.8}$$

Here $v_1(p,p',x,x')$ is the expression for the potential containing the integration over the azimuthal angle φ (We use the same notation as given in Ref. [13]),

$$v_1(q',q,x',x) = \int_0^\infty d\varphi\, V(q',q,x'x + \sqrt{1-x'^2}\,\sqrt{1-x^2}\cos\varphi). \tag{4.9}$$

In the case of the Malfliet-Tjon potential this integral can be performed analytically.

The values of $\langle H \rangle$, $\langle H_0 \rangle$, $\langle V \rangle$ are given in Table V for both potentials MT-V and MT-IV calculated in both schemes. One can see that the energy expectation values and eigenvalues $E_{\rm t}$ agree with high accuracy within each scheme as well as between the schemes.

V. VERIFICATION OF THE 3N SCHRÖDINGER EQUATION

In the previous sections we displayed properties of the 3N wave function, which we obtained from the Faddeev component by evaluating Eq. (2.18). We showed that the expectation value $\langle H \rangle$ evaluated with this wave function deviates from the calculated eigenvalue by less than 0.1%. However, since the expectation value is obtained by integrating over the wave function, this accuracy test gives information about the overall quality of the wave function. A more stringent test for the quality of $\Psi(p,q,x)$ at each point in the $p-q-x$ space is to determine the accuracy with which $\Psi(p,q,x)$ fulfills the 3N Schrödinger equation. To the best of our knowledge, such a test has never been carried out.

The 3N Schrödinger equation for the bound state of 3 identical particles is given in Eq. (2.1). Using the three different sets of Jacobi momenta in momentum space we obtain

$$\begin{aligned} E_{\rm t}\,\Psi(p_1,q_1,x_1) = & \left[\frac{1}{m}p_1^2 + \frac{3}{4m}q_1^2\right]\Psi(p_1,q_1,x_1) \\ & + \int_0^\infty dp_1'\,p_1^2 \int_{-1}^{1} dx_1'\,v_1(p_1,p_1',x_1,x_1')\,\Psi(p_1',q_1,x_1') \\ & + \int_0^\infty dp_2'\,p_2^2 \int_{-1}^{1} dx_2'\,v_2(p_2,p_2',x_2,x_2')\,\Psi(p_2',q_2,x_2') \\ & + \int_0^\infty dp_3'\,p_3^2 \int_{-1}^{1} dx_3'\,v_3(p_3,p_3',x_3,x_3')\,\Psi(p_3',q_3,x_3'). \end{aligned} \tag{5.1}$$

Here $v_i(p_i,p_i',x_i,x_i'), i=1,2,3$ contains the integration over the azimuthal angle φ in the different subsystems i (Eq. (4.9)). As an aside, in Ref. [15] this equation was used to obtain the eigenvalue $E_{\rm t}$ and the 3N wave function. We insert $\Psi(p,q,x)$ obtained from Eq. (2.18) and verify the equivalence of both sides of the Eq. (5.1). For the numerical evaluation of the integrals in Eq. (5.1) the z direction for each integral is chosen separately, so that always $\mathbf{q}_i$ points in the direction of z. Then the integration vectors $\mathbf{p}_i'$ are chosen with respect to $\mathbf{q}_i$ being the z-axis. The momenta $\mathbf{p}_i$ and $\mathbf{q}_i$, $i=2,3$ have to be expressed as functions of $\mathbf{p}_1$ and $\mathbf{q}_1$. From the definitions of the momentum vectors in Eq. (2.8) we obtain

$$\begin{aligned} \mathbf{q}_2 &= \mathbf{p}_1 - \tfrac{1}{2}\mathbf{q}_1 \\ \mathbf{p}_2 &= -\tfrac{1}{2}\mathbf{p}_1 - \tfrac{3}{4}\mathbf{q}_1 \\ \mathbf{q}_3 &= -\mathbf{p}_1 + \tfrac{1}{2}\mathbf{q}_1 \\ \mathbf{p}_3 &= -\tfrac{1}{2}\mathbf{p}_1 + \tfrac{3}{4}\mathbf{q}_1. \end{aligned} \tag{5.2}$$

The corresponding angles are defined as $x_i = \hat{\mathbf{p}}_i \cdot \hat{\mathbf{q}}_i$, where $i=2,3$. This leads to

$$x_2 = \frac{-p_1^2 + \frac{3}{4}q_1^2 - x_1 p_1 q_1}{\sqrt{p_1^2 + \frac{9}{4}q_1^2 + 3x_1 p_1 q_1}\sqrt{p_1^2 + \frac{1}{4}q_1^2 - x_1 p_1 q_1}}$$
$$x_3 = \frac{p_1^2 - \frac{3}{4}q_1^2 - x_1 p_1 q_1}{\sqrt{p_1^2 + \frac{9}{4}q_1^2 - 3x_1 p_1 q_1}\sqrt{p_1^2 + \frac{1}{4}q_1^2 + x_1 p_1 q_1}}. \tag{5.3}$$

Since the functional form of the integrals in Eq. (5.1) is the same, we only evaluate the first, which we can view as function of the momenta given in the coordinate system 1

$$\chi(p_1, q_1, x_1) = \int_0^\infty dp_1' \, p_1^2 \int_{-1}^{1} dx_1' \, v_1(p_1, p_1', x_1, x_1') \, \Psi(p_1', q_1, x_1'). \tag{5.4}$$

The two remaining integrals in Eq. (5.1) are then obtained by interpolating on $\chi(p_i, q_i, x_i)$, $i = 2, 3$ using the coordinate transformations given in Eqs. (5.2) and (5.3).

In Fig. 9 we display the relative error $\Delta = |(E\Psi(p,q,x) - H\Psi(p,q,x))|/|E\Psi(p,q,x)| \times 100$ for $x = -1$ for the wave function obtained from the MT-IV potential. The graph shows that the 3N Schrödinger equation is fulfilled with a numerical accuracy better than 1% for momenta p and q up to 6 fm^{-1}. This is a typical range of momenta which enters calculations of matrix elements, e.g., for electron scattering. When p exceeds values of 10 fm^{-1} the relative error becomes larger than 5% for almost all values of q. This behavior can be explained by inspecting the different Faddeev amplitudes separately as they are given in Eq. (2.19). If one considers the value $x = -1$ as shown in Fig. 9, one sees that for $p = 9.9$ fm^{-1} and $q = 10.3$ fm^{-1} the Faddeev amplitude ψ_2 is needed at a value $q_2 = 15.05$ fm^{-1}, which is outside the q-range the Faddeev equation was solved in this particular case. Instead of extrapolating, we set $\psi_2(p,q,x) = 0$, which introduces a small discontinuity in the wave function. Though not visible in integrations over the wave function, this leads to a larger error when considering the pointwise accuracy of the 3N Schrödinger equation. Of course, this larger error in $\Psi(p,q,x)$ is completely irrelevant in all practical cases, since for those large momenta p and q the wave function $\Psi(p,q,x)$ drops by about 8 orders of magnitude compared to its value at the origin. In the relevant momentum regions the 3N Schrödinger equation is fulfilled with very good accuracy by our three dimensional wave function. This statement holds for all x values.

For the above study we chose the wave function obtained from the MT-IV potential, since this wave function does not have any node lines. It is quite obvious that our definition of the relative error would give a large error at the locations where $\Psi(p,q,x)$ approaches zero. In fact, when calculating the relative error with the wave function obtained from the MT-V potential, we can identify the node lines of the wave function quite clearly.

VI. SUMMARY

An alternative approach to state-of-the-art three nucleon bound state calculations, which are based on solving the Faddeev equations in a partial wave truncated basis, is to work directly with momentum vector variables. We formulate the Faddeev equations for identical particles as function of vector Jacobi momenta, specifically the magnitudes of the momenta and the angle between them, and demonstrate their numerical feasibility and the accuracy

of their solutions. As two-body force we concentrated on a superposition of an attractive and repulsive Yukawa interaction, which is typical for nuclear physics, as well as on an attractive Yukawa interaction. The corresponding two-body t-matrix, which enters the Faddeev equations was also calculated as function of vector momenta. We neglected spin degrees of freedom in all our calculations.

As first test for the numerical accuracy of the solution of the Faddeev equation as function of vector variables, which is a three dimensional integral equation, we determined the energy eigenvalue of the bound system and compared our result with the one obtained in a traditional Faddeev calculation carried out in a partial wave truncated basis. We achieved excellent agreement between the two approaches as well as excellent agreement with calculations in the literature. We also found that the three dimensional Faddeev amplitude is nearly independent of the angle between the two Jacobi momenta. This is of course in agreement with the insights gained from the approach in the partial wave scheme.

From the Faddeev amplitude we obtained the 3N wave function. We found here also that the dependence on the angle between the two Jacobi momenta is quite weak. We then performed a partial wave decomposition of our three dimensional solutions for the Faddeev amplitude and the 3N wave function and compared the so obtained partial wave amplitudes with the ones directly calculated. Again we found excellent agreement between the two approaches. In order to further probe the quality of our wave function we calculated the momentum distributions $n(q)$ and $\hat{n}(p)$ and demonstrated that partial wave contributions up to $l = 12$ are necessary to build up the distribution $n(q)$ for large momentum transfers q. In a similar vain we showed that higher partial waves are needed to fill in the sharp dip in $\hat{n}(p)$, which is obtained in a pure s-wave calculation.

For a stringent test of the three dimensional wave function we inserted it into the 3N Schrödinger equation and evaluated the accuracy with which the eigenvalue equation is fulfilled throughout the entire space where the solution is defined. We found that within the physical relevant momentum region, namely p and q less than 10 fm^{-1}, the 3N Schrödinger equation is fulfilled with high accuracy by our numerical solution of the Faddeev equation.

Summarizing we can state that the three dimensional Faddeev equation for a bound state can be handled in a straightforward and numerically reliable fashion. Once supplemented by spin degrees of freedom, this approach will most likely be more easily implemented than the traditional partial wave based method. State-of-the-art bound state calculations with realistic nuclear force models typically require at least 34 channels. The incorporation of 3N forces will most likely also be less cumbersome in a three dimensional approach.

ACKNOWLEDGMENTS

This work was performed in part under the auspices of the U. S. Department of Energy under contract No. DE-FG02-93ER40756 with Ohio University, the NATO Collaborative Research Grant 960892, the National Science Foundation under Grant No. INT-9726624 and the Deutsche Forschungsgemeinschaft under Grant GL-8727-1. We thank the Ohio Supercomputer Center (OSC) for the use of their facilities under Grant No. PHS206, the National Energy Research Supercomputer Center (NERSC) for the use of their facilities under the FY1998 Massively Parallel Processing Access Program and the Höchstleistungsrechenzentum Jülich for the use of their Cray-T3E. The authors would like to thank H. Kamada for many stimulating and fruitful discussions.

APPENDIX A: EXPLICIT REPRESENTATION OF THE PARTIAL WAVE PROJECTED PERMUTATION OPERATOR

For the convenience of the reader we provide the quantities G and $\tilde{G}$ related to the permutation operators for general total angular momentum L.

The function $G_{ll'}(q,q',x')$ from Eq. (2.15) is a combination of Legendre polynomials $P_k(x)$:

$$G_{l\lambda,l'\lambda'}(q,q',x) = \sum_k P_k(x) \sum_{\mu_1+\mu_2=l} \sum_{\nu_1+\nu_2=l'} q'^{\mu_1+\nu_2}\; q^{\mu_2+\nu_1}\; g^{k\mu_1\nu_1\mu_2\nu_2}_{l\lambda,l'\lambda'}. \tag{A1}$$

For general L the geometrical coefficient is given as

$$\begin{aligned} g^{k\mu_1\nu_1\mu_2\nu_2}_{l\lambda,l'\lambda'} &= \sum_{gg'} \hat{k}\,\sqrt{\hat{l}\hat{\lambda}\hat{l}'\hat{\lambda}'}\,\sqrt{\frac{\hat{l}!\hat{l}'!}{(2\mu_1)!\,(2\mu_2)!\,(2\nu_1)!\,(2\nu_2)!}} \\ &\quad\times (-)^{l'}\left(\tfrac{1}{2}\right)^{\mu_2+\nu_2} \left\{\begin{array}{ccc} \mu_1 & \mu_2 & l \\ \lambda & L & g \end{array}\right\} \left\{\begin{array}{ccc} \nu_1 & \nu_2 & l' \\ \lambda' & L & g' \end{array}\right\} \left\{\begin{array}{ccc} \mu_1 & g & L \\ \nu_1 & g' & k \end{array}\right\} \\ &\quad\times C(\mu_2\;\lambda\;g,0\;0)\;C(\nu_2\;\lambda'\;g',0\;0)\;C(k\;\nu_1\;g,0\;0)\;C(k\;\mu_1\;g',0\;0). \end{aligned} \tag{A2}$$

Here l and λ are the relative orbital angular momenta related to p and q. We also use the notation $\hat{l} \equiv 2l+1$.

In our context we have $L=0$, which leads to $l=\lambda$. Then g reduces to

$$\begin{aligned} g^{k\mu_1\nu_1\mu_2\nu_2}_{ll'} &= \sqrt{\frac{\hat{l}\hat{l}'}{\hat{\mu}_1\;\hat{\nu}_1}}\;\sqrt{\frac{\hat{l}!\hat{l}'!}{(2\mu_1)!\,(2\mu_2)!\,(2\nu_1)!\,(2\nu_2)!}} \\ &\quad\times \left(\tfrac{1}{2}\right)^{\mu_2+\nu_2}\;(-)^{\mu_1+\nu_1} C(\mu_2\;l\;\mu_1,0\;0)\;C(\nu_2\;l'\;\nu_1,0\;0)\;C(\mu_1\;\nu_1\;k,0\;0)^2 \end{aligned} \tag{A3}$$

and $G_{l\lambda,l'\lambda'}$ to $G_{ll'}$.

The quantity $\tilde{G}(p,q,x)$ occurs in Eq. (2.24). In the case of general L the function $\tilde{G}$ reads

$$\tilde{G}_{l\lambda,l'\lambda'}(p,q,x) = \sum_k P_k(x) \sum_{\mu_1+\mu_2=l'} \sum_{\nu_1+\nu_2=\lambda'} p^{\mu_1+\nu_1}\; q^{\mu_2+\nu_2}\; \tilde{g}^{k\mu_1\nu_1\mu_2\nu_2}_{l\lambda,l'\lambda'} \tag{A4}$$

with the geometrical factor

$$\tilde{g}^{k\mu_1\nu_1\mu_2\nu_2}_{l\lambda,l'\lambda'} = \sum_{gg'} \hat{k}\,\sqrt{\hat{l}'\hat{\lambda}'\hat{g}\hat{g}'}\sqrt{\frac{\hat{l}'!\hat{\lambda}'!}{(2\mu_1)!\,(2\mu_2)!\,(2\nu_1)!\,(2\nu_2)!}}$$
$$\times(-)^{g+L+\nu_2}\left(\tfrac{1}{2}\right)^{\mu_1+\nu_2}\left(\tfrac{3}{4}\right)^{\mu_2}\left\{\begin{array}{ccc}\mu_1 & \mu_2 & l'\\ \nu_1 & \nu_2 & \lambda'\\ g & g' & L\end{array}\right\}\left\{\begin{array}{ccc}g' & g & L\\ l & \lambda & k\end{array}\right\}$$
$$\times C(\mu_1\ \nu_1\ g,0\ 0)\ C(\mu_2\ \nu_2\ g',0\ 0)\ C(g\ k\ l,0\ 0)\ C(g'\ k\ \lambda,0\ 0). \qquad \text{(A5)}$$

Again, for $L=0$ $\tilde{g}$ reduces to

$$\tilde{g}^{k\mu_1\nu_1\mu_2\nu_2}_{ll'} = \sum_{g} \hat{k}\,(-)^{\mu_2+g+k}\left(\tfrac{1}{2}\right)^{\mu_1+\nu_2}\sqrt{\frac{\hat{l}'}{\hat{l}}}\sqrt{\frac{\hat{l}'!\hat{\lambda}'!}{(2\mu_1)!\,(2\mu_2)!\,(2\nu_1)!\,(2\nu_2)!}}$$
$$\times\left(\tfrac{3}{4}\right)^{\mu_2}\left\{\begin{array}{ccc}\mu_1 & \mu_2 & l'\\ \nu_2 & \nu_1 & g\end{array}\right\}\ C(\mu_1\ \nu_1\ g,0\ 0)\ C(\mu_2\ \nu_2\ g,0\ 0)\ C(g\ k\ l,0\ 0)^2 \qquad \text{(A6)}$$

and correspondingly $\tilde{G}_{l\lambda,l'\lambda'}$ to $\tilde{G}_{ll'}$.

REFERENCES

[1] A. Picklesimer, R.A. Rice, and R. Brandenburg, Phys. Rev C **45**, 2045 (1992), *ibid*, 547 (1992), Phys. Rev. C **44**, 1359 (1991).

[2] A. Stadler, W. Glöckle, P.U. Sauer, Phys. Rev. C **44**, 2319 (1991); A. Stadler and P.U. Sauer, Phys. Rev. C **46**, 64 (1992).

[3] A. Nogga, D. Hüber, H. Kamada, W. Glöckle, Phys. Lett. B **409**, 19 (1997).

[4] J.L. Friar, B.F. Gibson, and G.L. Payne, Z. Phys. **A 301**, 309 (1981), C.R. Chen, G.L. Payne, J.L. Friar, B.F. Gibson, Phys. Rev. C **31**, 2266 (1985).

[5] N.W. Schellingerhout, L.P. Kok, and G.D. Bosveld, Phys. Rev. A **40**, 5568 (1989); N.W. Schellingerhout, J.J. Schut, and L.P. Kok, Phys. Rev. C **46**, 1192 (1992).

[6] Y. Wu, S. Ishikawa, T. Sasakawa, Few-Body Systems **15**, 145 (1993).

[7] A. Arriaga, V.R. Pandharipande, R.B. Wiringa, Phys. Rev. C **52**, 2362 (1995).

[8] J. Carlson, Phys. Rev. C **36**, 2026 (1987), Phys. Rev. C **38**, 1879 (1988); J.G. Zabolitzki, K.E. Schmidt, and M.H. Kalos, Phys. Rev. C **25**, 1111 (1982); J. Carlson and R. Schiavilla, to appear in Rev. Mod. Phys.

[9] A.A. Kvitsinsky and C.-Y. Hu, Few-Body Systems **12**, 7 (1992).

[10] M. Viviani, A. Kievski, and S. Rosati, Nuovo Cim. **105A**, 1473 (1992).

[11] A. Kievsky, L.E. Marcucci, S. Rosati, and M. Viviani, Few-Body Systems **22**, 1 (1997); S. Rosati, M. Viviani, A. Kievsky, Few-Body Systems, Suppl. 8, 21 (1995).

[12] H. Kameyama, M. Kamimura, and Y. Fukushima, Phys. Rev. C **40**, 974 (1989); M. Kamimura and H. Kameyama, Nucl. Phys. **A508**, 17c (1990).

[13] Ch. Elster, J.H. Thomas, and W. Glöckle, to appear in Few-Body Systems.

[14] R. Machleidt, K. Holinde, Ch. Elster, Phys. Rep. **149**, 1 (1987).

[15] O. Kalusch and W. Glöckle, Few-Body Systems **5**, 79 (1988).

[16] W. Glöckle, The Quantum Mechanical Few-Body Problem, Springer Verlag, 1983.

[17] D. Hüber, H. Witala, W. Glöckle, Few-Body Systems **14**, 171 (1993).

[18] R.A. Malfliet and J.A. Tjon, Nucl. Phys. **A127**, 161 (1969).

[19] N.W. Schellingerhout, *Factorizability in the Numerical Few-Body Problem*, Ph.D. Thesis, Rijksuniversiteit Groningen, 1995.

[20] W. Glöckle in *Computational Nuclear Physics*, Vol. 1, Eds. K. Langanke, J.A. Marun, and S.E. Koonin, Springer Verlag 1991, p.152.

[21] D. Hüber, H. Witala, A. Nogga, W. Glöckle, and H. Kamada, Few Body Systems **22**, 107 (1997).

[22] C. de Boor in *A Practical Guide to Splines*, Springer, N.Y., 1978.

TABLES

TABLE I. Parameters of the Malfliet-Tjon type potentials. As conversion factor we use units such that $\hbar c = 197.3$ MeV fm $= 1$. We also use $\hbar^2/m = 41.470$ MeV fm^2.

	$V_{\rm A}$ [MeV fm]	$\mu_{\rm A}$ [fm^{-1}]	$V_{\rm R}$ [MeV fm]	$\mu_{\rm R}$ [fm^{-1}]
MT-V	-570.3316	1.550	1438.4812	3.11
MT-IV	-65.1090	0.633	-	-

TABLE II. The calculated eigenvalue $E_{\rm t}$ of the Faddeev equation as function of the number of grid points NP1, NP2, NQ1, NQ2, and NX chosen for the solution of Eq. (2.14). The calculations are based on the potentials MT-V and MT-IV.

NP1	NP2	NQ1	NQ2	NX	$E_{\rm t}$ [MeV] (MT-V)	$E_{\rm t}$ [MeV] (MT-IV)
20	12	20	12	40	-7.74387	-25.0416
24	24	24	16	40	-7.74000	-25.0453
32	24	24	16	40	-7.73761	-25.0485
32	24	32	16	40	-7.73761	-25.0483
32	24	32	32	40	-7.73761	-25.0483
32	32	32	32	40	-7.73761	-25.0483
48	32	48	32	40	-7.73666	-25.0499
64	32	48	32	40	-7.73666	-25.0502
64	32	64	32	40	-7.73650	-25.0502
72	36	64	32	40	-7.73650	-25.0499

TABLE III. The calculated eigenvalue $E_{\rm t}$ of the Faddeev equation as function of the number of partial waves employed. A fixed set of grid points is chosen corresponding to NP1 = 64, NP2 = 32, NQ1 = 64, NQ2 = 32, NX = 16. The partial wave t-matrix is calculated on a larger grid of 160×160 grid points. The calculations are based on the potentials MT-V and MT-IV.

l	$E_{\rm t}$ [MeV] (MT-V)	$E_{\rm t}$ [MeV] (MT-IV)
0	-7.53975	-24.8616
2	-7.71470	-25.0465
4	-7.73383	-25.0552
6	-7.73613	-25.0562
8	-7.73649	-25.0564
10	-7.73656	-25.0565
12	-7.73658	-25.0565

TABLE IV. The relative contributions of the partial wave Faddeev amplitudes F_l for each partial wave. We give also the corresponding values W_l for the wave function. The calculations are based on the potentials MT-V and MT-IV.

	MT-V		MT-IV	
l	F_l	W_l	F_l	W_l
0	99.9951	99.0851	99.9940	99.2121
2	$0.4823 \cdot 10^{-2}$	0.7482	$0.5923 \cdot 10^{-2}$	0.7318
4	$0.7988 \cdot 10^{-4}$	0.1159	$0.3128 \cdot 10^{-4}$	$0.4682 \cdot 10^{-1}$
6	$0.2278 \cdot 10^{-5}$	$0.3305 \cdot 10^{-1}$	$0.8813 \cdot 10^{-6}$	$0.6743 \cdot 10^{-2}$
8	$0.1110 \cdot 10^{-6}$	$0.1088 \cdot 10^{-1}$	$0.6056 \cdot 10^{-7}$	$0.1520 \cdot 10^{-2}$
10	$0.8677 \cdot 10^{-8}$	$0.3939 \cdot 10^{-2}$	$0.7156 \cdot 10^{-8}$	$0.4528 \cdot 10^{-3}$
12	$0.1006 \cdot 10^{-8}$	$0.1545 \cdot 10^{-2}$	$0.1147 \cdot 10^{-8}$	$0.1627 \cdot 10^{-3}$

TABLE V. The expectation value $\langle H \rangle$, $\langle H_0 \rangle$, and $\langle V \rangle$ calculated for the potentials MT-V and MT-IV within the three dimensional scheme (3D) and the partial wave scheme (PW).

		$\langle H_0 \rangle$ [MeV]	$\langle V \rangle$ [MeV]	$\langle H \rangle$ [MeV]	$(E_{\rm t} - \langle H \rangle)$ [MeV]
MT-V	3D	29.77706	-37.51340	-7.73634	0.00011
	PW	29.7776	-37.5139	-7.73634	0.00024
MT-IV	3D	77.2055	-102.2550	-25.0495	0.0003
	PW	77.2653	-102.3207	-25.0554	0.0011

FIGURES

FIG. 1. The angular dependence for the symmetrized off-shell t-matrix, $t_{\rm s}(p,p',x,E)$, is displayed for $p = 0.75$ fm^{-1} and $E = -50$ MeV.

FIG. 2. The magnitude of the Faddeev component $\psi(p,q,x)$ for $x = 1$ calculated from the MT-V potential.

FIG. 3. The partial wave projected Faddeev components $\psi_l(p,q)$ calculated from the MT-V potential are shown for $l = 0, 2, 4$. The left column of graphs represents the amplitudes obtained from the three dimensional calculations. Here (a) stands for the $l = 0$ amplitude, (b) the one for $l = 2$, and (c) the one for $l = 4$. The amplitudes in the right column are obtained as solutions of the partial wave Faddeev equation, (d) represent the $l = 0$ amplitude, (e) the one for $l = 2$, and (f) the one for $l = 4$.

FIG. 4. The magnitude of the 3N bound state wave function $\Psi(p,q,x)$ for $x = 1$ calculated from the MT-V potential.

FIG. 5. The partial wave projected bound state wave functions $\Psi_l(p,q)$ calculated from the MT-V potential are show for $l = 0, 2, 4$. The left column of graphs represents the amplitudes obtained from the three dimensional calculations. Here (a) stands for the $l = 0$ amplitude, (b) the one for $l = 2$, and (c) the one for $l = 4$. The amplitudes in the right column are obtained as solutions of the partial wave Faddeev equation, (d) represent the $l = 0$ amplitude, (e) the one for $l = 2$, and (f) the one for $l = 4$.

FIG. 6. The magnitude of the 3N bound state wave function $\Psi(p,q,x)$ for $x = 1$ calculated from the MT-IV potential.

FIG. 7. The momentum distribution $n(q)$ is shown in (a) for the MT-V potential as calculated in the two different schemes. The solid line refers shows the result from the three dimensional calculation whereas the dashed line gives the result from the partial wave sum up to $l = 12$. The monotonic increasing partial wave sums for $l = 0, 2, 4, 6, 8, 10,$ and 12 are shown in (b).

FIG. 8. The momentum distribution $\hat{n}(p)$ is shown in (a) for the MT-V potential as calculated in the two different schemes. The solid line refers shows the result from the three dimensional calculation whereas the dashed line gives the result from the partial wave sum up to $l = 12$. The monotonic increasing partial wave sums for $l = 0, 2, 4, 6, 8, 10,$ and 12 are shown in (b).

FIG. 9. The relative error Δ as defined in the text as function of the momenta p and q for the fixed angle $x = -1$ represents a measure for the accuracy with which the 3N Schrödinger equation is fulfilled by the three dimensional wave function obtained from the MT-IV potential. The numbers at the contour lines give the relative error in %.

Fig. 1

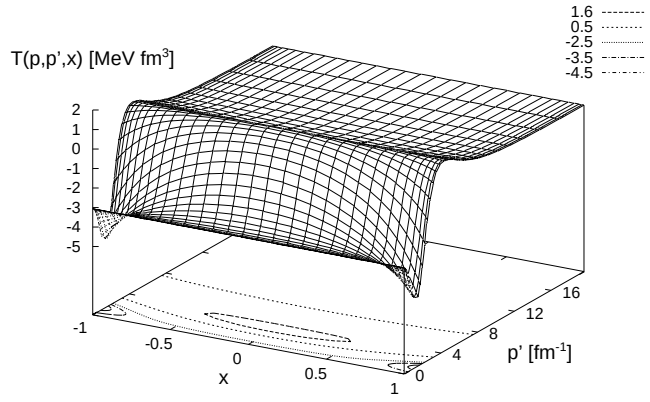
T(p,p',x) [MeV fm^3]
1.6
0.5
-2.5
-3.5
-4.5
2
1
0
-1
-2
-3
-4
-5
-1
-0.5
0
0.5
1
x
0
4
8
12
16
p' [fm^{-1}]

Fig. 2

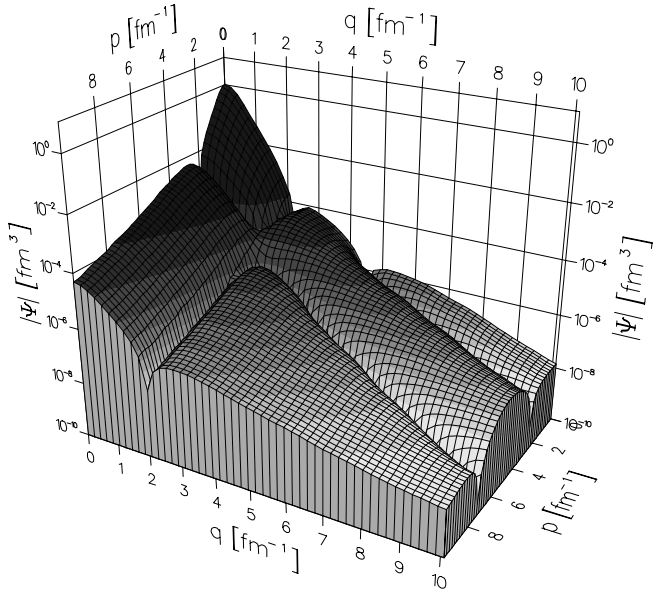
p [fm^{-1}]
q [fm^{-1}]
|Ψ| [fm^3]
10^0
10^{-2}
10^{-4}
10^{-6}
10^{-8}
0
1
2
3
4
5
6
7
8
9
10

3D calculation partial wave calculation Fig. 3

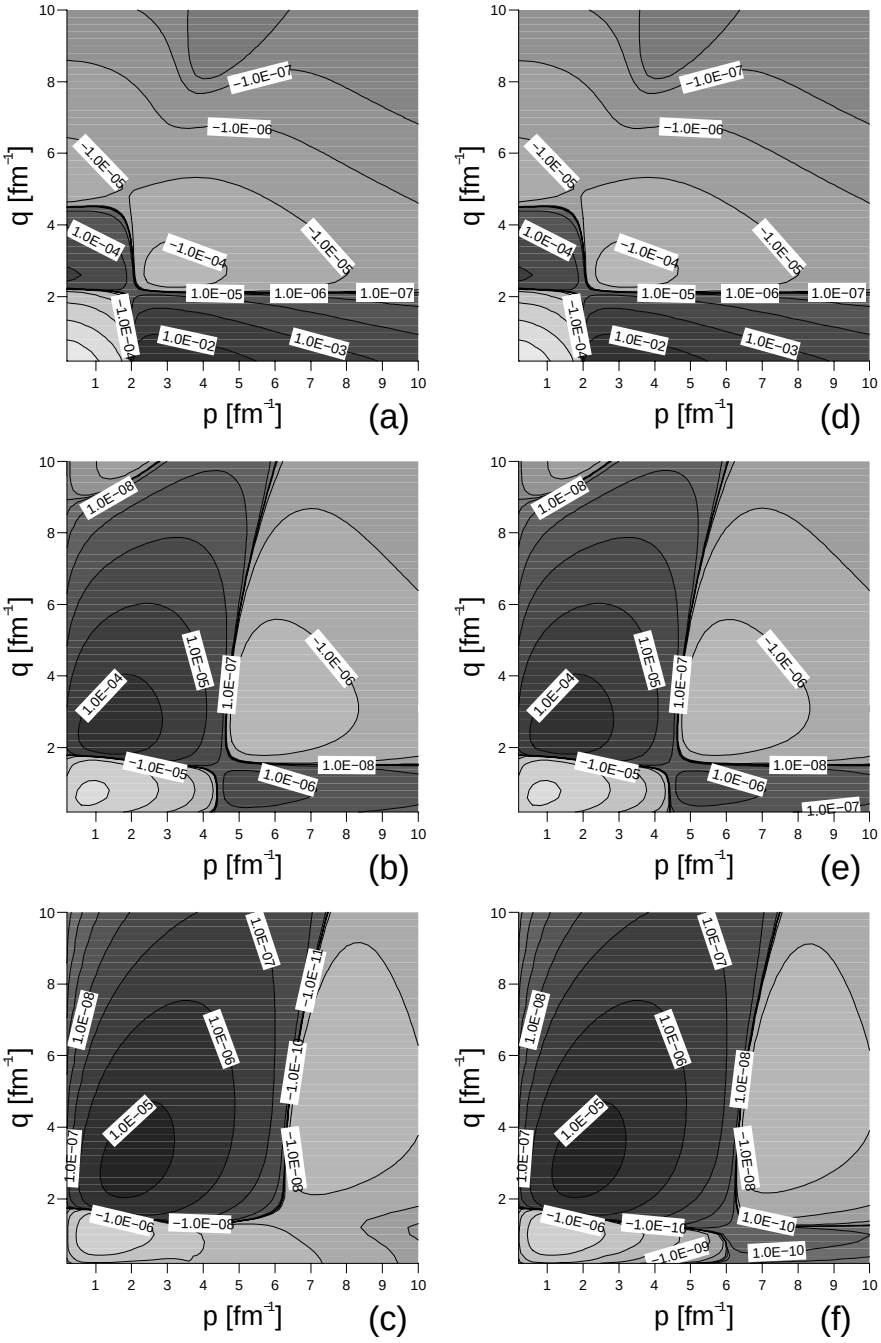

Fig. 4

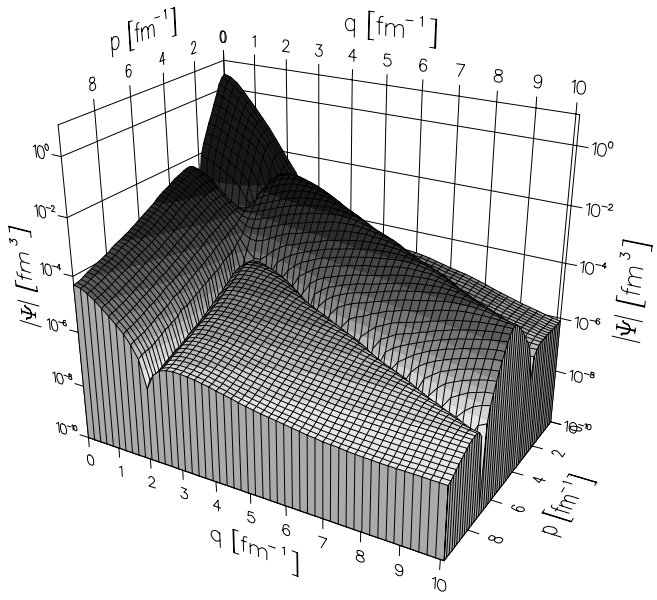

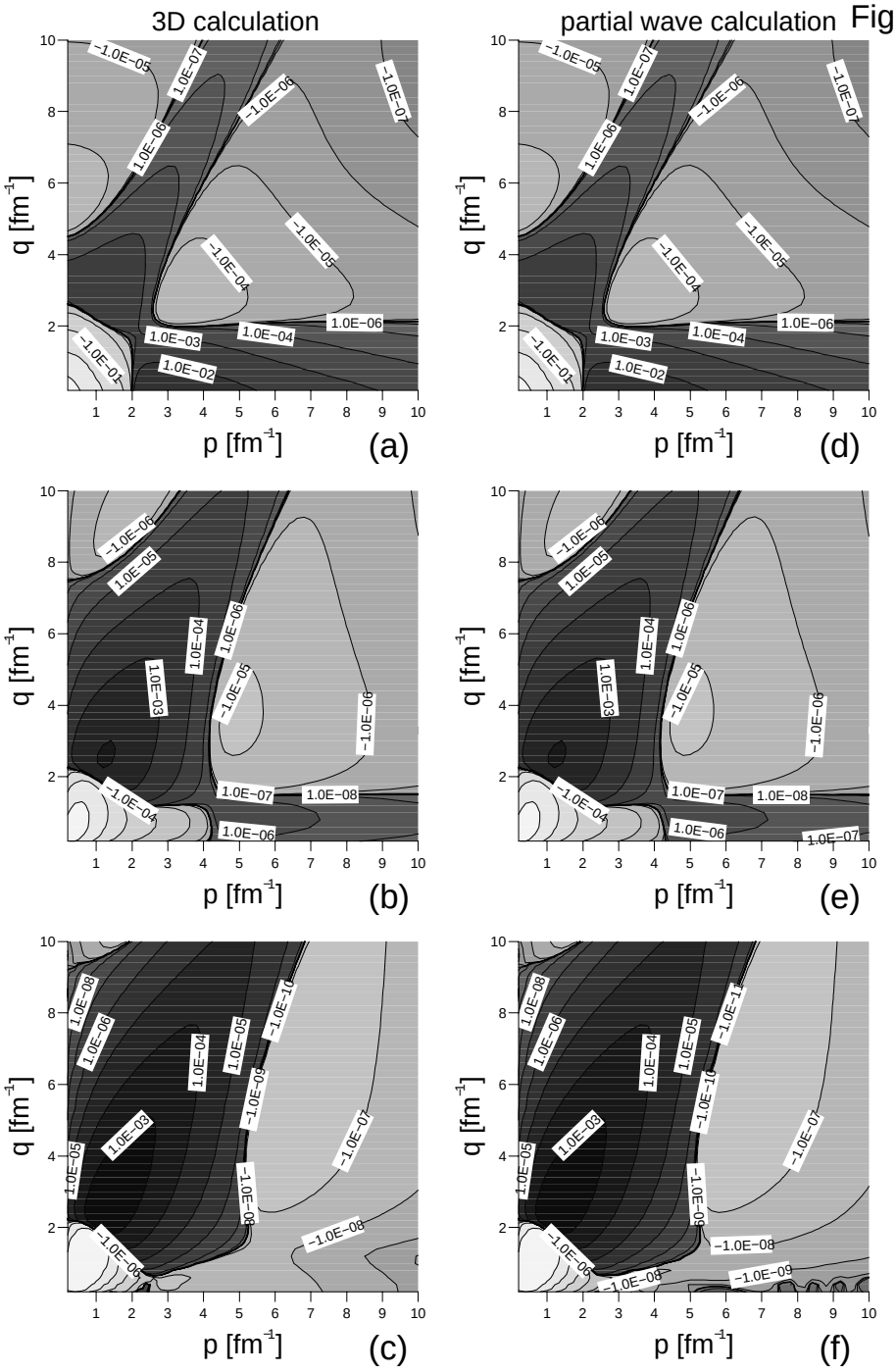
3D calculation
partial wave calculation
Fig. 5
q [fm^{-1}]
p [fm^{-1}]
(a)
(b)
(c)
(d)
(e)
(f)

Fig. 6

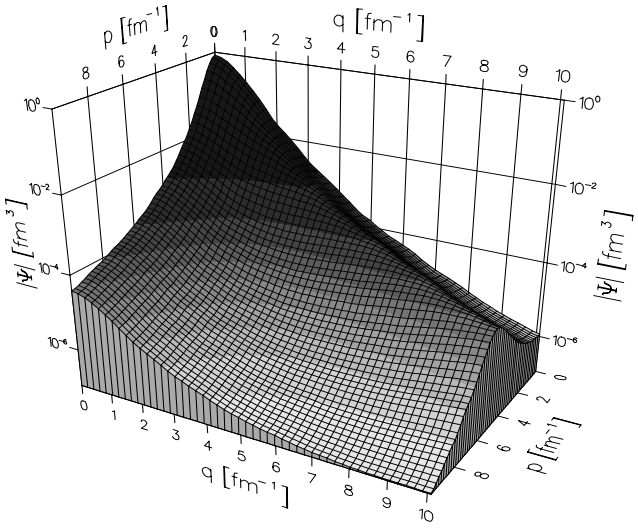

Fig. 7

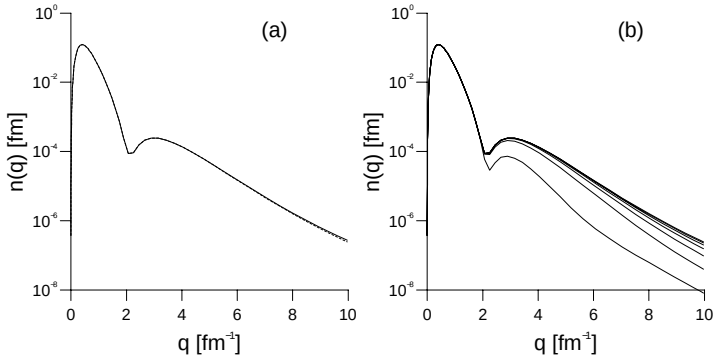

Fig. 8

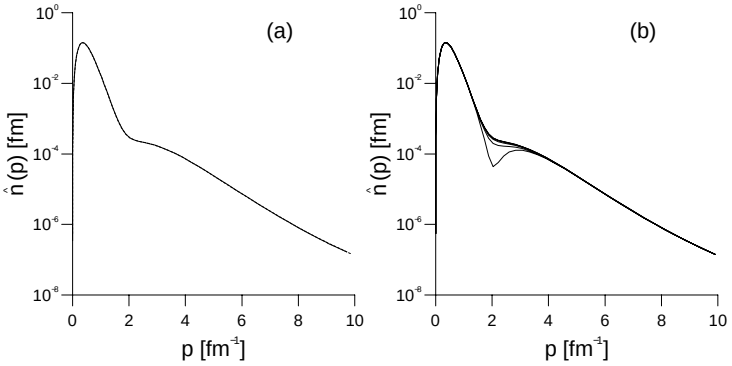
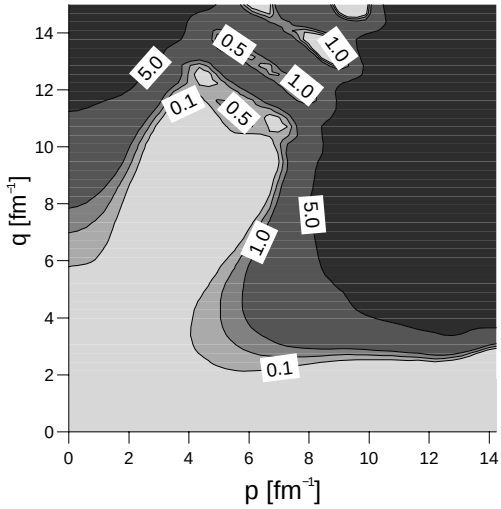
Fig. 9